Comput Mech (2007) 40:281–298
DOI 10.1007/s00466-006-0097-y

ORIGINAL PAPER

A numerical method for homogenization in non-linear elasticity

I. Temizer · T. I. Zohdi

Received: 19 March 2006 / Accepted: 15 June 2006 / Published online: 20 July 2006

Abstract In this work, homogenization of heterogeneous materials in the context of elasticity is addressed, where the effective constitutive behavior of a heterogeneous material is sought. Both linear and non-linear elastic regimes are considered. Central to the homogenization process is the identification of a statistically representative volume element (RVE) for the heterogeneous material. In the linear regime, aspects of this identification is investigated and a numerical scheme is introduced to determine the RVE size. The approach followed in the linear regime is extended to the non-linear regime by introducing stress–strain state characterization parameters. Next, the concept of a material map, where one identifies the constitutive behavior of a material in a discrete sense, is discussed together with its implementation in the finite element method. The homogenization of the non-linearly elastic heterogeneous material is then realized through the computation of its effective material map using a numerically identified RVE. It is shown that the use of material maps for the macroscopic analysis of heterogeneous structures leads to significant reductions in computation time.

Keywords Homogenization · Elasticity · Micromechanics

1 Introduction

Heterogeneous materials have physical properties that vary throughout their microstructures. The subject of *homogenization* is to determine the "apparent" (or, "overall") physical properties of a heterogeneous material, thereby allowing one to substitute this material with an effectively equivalent homogeneous material (Fig. 1). Typically, the overall property sought is an effective constitutive equation, such as one relating stress to strain. The ability to replace the heterogeneous material with an effective homogeneous material greatly reduces the computational effort required for the solution of a problem posed over the macroscopic structure domain.

In this work, the problem of homogenization is addressed in the context of elasticity. Both linear and non-linear elastic regimes are considered. Homogenization analysis in the linear elastic regime is well-established. See [1,4,6,18,20,26,28] for reviews of analytical and computational methods. The homogenization procedure involves the analysis of a statistically representative volume element (RVE) from the heterogeneous material, and the result is an estimate or a set of bounds for the elasticity tensor. Analytical bounds are typically coarse, and therefore computational methods have been developed that provide arbitrarily refinable bounds. These computational methods rely on the proper identification of a finite sized RVE. See [12,23] for examples.

Homogenization in the non-linear elastic regime is a much less developed field. An analytical approach to the problem involves constructing bounds on the effective strain energy. See, for instance, [3,17,21,25,27]. However, non-uniqueness of the solution at finite deformations, the nature of the strain energy function (such as non-convexity), and non-invertability of the stress-strain relationship render these results applicable only in a range of deformations or for a limited class of materials. Accordingly, computational approaches have recently been developed where one operates on a finite sized

I. Temizer (✉) · T. I. Zohdi
Department of Mechanical Engineering,
University of California, Berkeley, CA 94720-1740, USA
e-mail: temizer@ibnm.uni-hannover.de

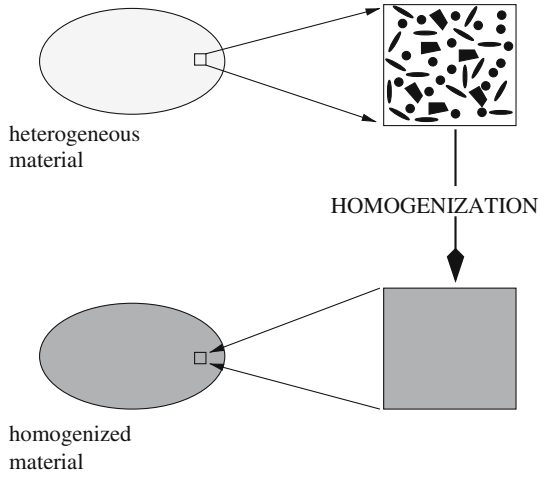

Fig. 1 Homogenization of a heterogeneous material

RVE of the heterogeneous material to extract effective stress/strain at a point of the macroscopic structure. See [2,13,15] and references therein. Although these methods are applicable to a wide range of material behavior (such as elasticity, plasticity and damage mechanics), they are computationally very demanding, requiring several RVE analyses for each element of the finite element mesh.

Here, aspects of computational methods for linear and non-linear elasticity are investigated. Central to any micromechanical analysis of heterogeneous materials is the proper identification of an RVE. Therefore, first a method for the numerical determination of an RVE is introduced in the linear elastic regime, and analyzed using a specific homogenization problem. This method is then extended to the non-linear elastic regime in a way that simplifies to the linear elastic regime procedure as a special case. Also, a numerical method for homogenizing heterogeneous materials undergoing non-linearly elastic deformations is developed, based on the method of identifying a suitable RVE. In particular a *discrete material map* is constructed, which characterizes the effective stress-strain relationship for the heterogeneous material, and its implementation in a numerical framework is discussed. This material map essentially provides a constitutive formulation, which can now be used in a structural analysis where the structural material is characterized by its material map, leading to significant reductions in computation time.

2 Homogenization problem

In this section, the homogenization problem is introduced in the context of elasticity. Consider a heterogeneous material $\mathcal{M}$ associated with the reference configuration $\mathcal{R}_o$ for which the constitutive equation is $\boldsymbol{\sigma} = \widehat{\boldsymbol{\sigma}}(\boldsymbol{X}, \boldsymbol{\epsilon})$. Here, $\boldsymbol{\sigma}$ and $\boldsymbol{\epsilon}$ denote, respectively, the stress and strain tensors in linear elasticity, and $\boldsymbol{X}$ is the position vector for $\mathcal{R}_o$. In this work, attention is focused to quasistatic problems posed for heterogeneous materials which are composed of two constituents (Fig. 2), a matrix ($\mathcal{M}^1$) and monodispersed spherical particles ($\mathcal{M}^2$). [1] In linear elasticity, each constituent is characterized by its elasticity tensor $\mathbb{E}^I$. The number of particles is denoted by N_p, and their volume fraction by v_o^2.

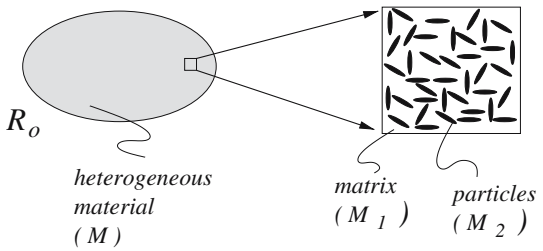

Fig. 2 Heterogeneous material composed of a matrix and particles

The number of particles in $\mathcal{R}_o$ is typically very large. The number of degrees of freedom needed in a numerical analysis in order to capture the solution position vector $\boldsymbol{x}(\boldsymbol{X})$ to the heterogeneous problem accurately by resolving the microstructure to sufficient detail is then also extremely large. Therefore, it is desirable to seek an approximate solution $\boldsymbol{x}^*(\boldsymbol{X})$ to the boundary value problem for $\mathcal{M}$ by replacing it with a homogeneous material $\mathcal{M}^*$.[2] If this material also undergoes linear deformations, it is completely characterized by its elasticity tensor $\mathbb{E}^*$.[3] Since $\mathcal{M}^*$ is homogeneous, the numerical concerns are reduced to standard accuracy concerns that are independent of a microstructure. Therefore, the problem on the heterogeneous material has been reduced to accurate homogenization, i.e. the identification of material $\mathcal{M}^*$ through the estimation of $\mathbb{E}^*$, which is referred to as the *effective*, *macroscopic*, *apparent*, or *overall* property in the literature.

A key concept in the determination of $\mathbb{E}^*$ is a statistically representative volume element (RVE). Consider a *volume element* $\mathcal{V}_o \subset \mathcal{R}_o$ that represents a sample from the heterogeneous material (Fig. 3). Although

[1] Monodispersed particles have the same size and shape, versus polydispersed particles which may have varying shape and size. See [24] for a treatise on the physical properties and manufacturing details of a class of such materials.

[2] The notation (.)* should be understood to represent the homogeneous equivalent of the heterogeneous problem quantity (.). Therefore, no explicit definitions are given for (.)* quantities.

[3] The underlying assumption is that the distribution of particles thoroughout the macroscopic structure is uniform.

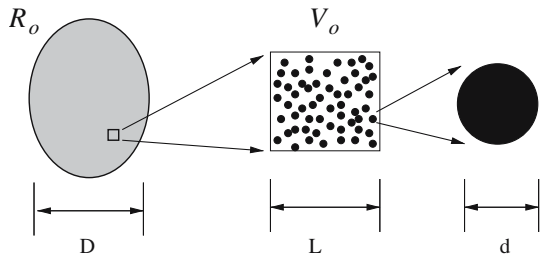

Fig. 3 The "micro-meso-macro" principle of homogenization

various identifications of an RVE are available in the literature,[4] a common requirement is that the typical dimension of the particles (d) be much smaller than the typical dimension of $\mathcal{V}_o$ (L): $d \ll L$. In the limit as $d/L \to 0$, the sample would be expected to resemble a homogeneous material macroscopically. This is the intuition on which the calculation of effective properties is based. On the other hand, applicability of homogenization to a microscopically heterogeneous (macro)structure requires that the RVE size (L) be much smaller than the typical dimension of the macrostructure (D): $L \ll D$. The principle $d \ll L \ll D$ is also referred to as the "micro-meso-macro principle" [8], where "micro", "meso" and "macro" refer to the microstructure, RVE size, and macrostructure, respectively.

Using a volume element $\mathcal{V}_o$ that qualifies as an RVE, $\mathbb{E}^*$ is typically calculated by subjecting $\mathcal{V}_o$ to special boundary conditions and relating the average stress[5] $\langle\boldsymbol{\sigma}\rangle_{\mathcal{V}_o}$ to the average strain $\langle\boldsymbol{\epsilon}\rangle_{\mathcal{V}_o}$ through the relationship $\langle\boldsymbol{\sigma}\rangle_{\mathcal{V}_o} = \mathbb{E}^*\langle\boldsymbol{\epsilon}\rangle_{\mathcal{V}_o}$. For volume elements (or, *samples*) with a given number of particles that are smaller than the *RVE* size, relating $\langle\boldsymbol{\sigma}\rangle_{\mathcal{V}_o}$ to $\langle\boldsymbol{\epsilon}\rangle_{\mathcal{V}_o}$ only yields an approximation to $\mathbb{E}^*$. One type of special boundary condition typically used is the *linear displacement* boundary condition, where the solution vector is prescribed as $\boldsymbol{x} = \boldsymbol{X} + \boldsymbol{\mathcal{E}}\boldsymbol{X}$ on $\partial\mathcal{V}_o$, which yields an estimate $\mathbb{E}_{\boldsymbol{\mathcal{E}}}$ to $\mathbb{E}^*$. The second type of boundary condition is the *uniform traction* boundary condition, where the traction vector is prescribed as $\boldsymbol{p} = \boldsymbol{\Sigma}\boldsymbol{N}$ on $\partial\mathcal{V}_o$, which yields an estimate $\mathbb{C}_{\boldsymbol{\Sigma}}$ to $\mathbb{C}^* = (\overset{\text{def}}{=} \mathbb{E}^*)^{-1}$. In these equations, $\boldsymbol{\mathcal{E}}$ and $\boldsymbol{\Sigma}$ are constant tensors. These boundary conditions satisfy *Hill's energy criterion*, so that $\langle\boldsymbol{\sigma}\cdot\boldsymbol{\epsilon}\rangle_{\mathcal{V}_o} = \langle\boldsymbol{\sigma}\rangle_{\mathcal{V}_o}\cdot\langle\boldsymbol{\epsilon}\rangle_{\mathcal{V}_o}$. In words, this equality states that in the transition from the microscopic scale to the macroscopic scale, energy is conserved.

[4] See [23] for examples.

[5] The *volume average* of a quantity $\mathcal{Q}$ with respect to a domain Ψ is defined as $\langle\mathcal{Q}\rangle_\Psi \overset{\text{def}}{=} (1/|\Psi|)\int_\Psi \mathcal{Q}\,\mathrm{d}\Psi$.

2.1 Numerical RVE size

In this work, macroscopically isotropic materials are considered, therefore the two linear elastic constants (bulk and shear moduli) describing the form of $\mathbb{E}^*$ can be computed using:[6]

$$\kappa^* = \frac{\operatorname{tr}\left(\langle\boldsymbol{\sigma}\rangle_{\mathcal{V}_o}\right)}{3\operatorname{tr}\left(\langle\boldsymbol{\epsilon}\rangle_{\mathcal{V}_o}\right)}, \qquad \mu^* = \frac{\left\|\langle\boldsymbol{\sigma}\rangle'_{\mathcal{V}_o}\right\|}{2\left\|\langle\boldsymbol{\epsilon}\rangle'_{\mathcal{V}_o}\right\|}, \tag{1}$$

if $\mathcal{V}_o$ is an RVE, where $(.)'$ denotes the deviatoric part. For small samples, one may compute $\{\kappa_{\boldsymbol{\mathcal{E}}}, \mu_{\boldsymbol{\mathcal{E}}}\}$ and $\{\kappa_{\boldsymbol{\Sigma}}, \mu_{\boldsymbol{\Sigma}}\}$, with obvious definitions, as estimates to $\{\kappa^*, \mu^*\}$ using linear displacement and uniform traction boundary conditions. By computing these parameters for small samples that are typically not isotropic, one introduces an error which will be referred to as *isotropic inconsistency*. However, large samples typically display negligible anisotropy. This issue will be revisited shortly.

Macroscopically isotropic particulate composites is achieved by random particle distribution at the microscale.[7] Therefore, for a given sample size,[8] multiple distributions of particles are possible. In order to capture a statistical measure of the range of responses from different distributions, one may use *ensemble averaging*. For a given sample size, ensemble averaging over N samples is defined by[9]

$$\begin{aligned}
&\langle\!\langle\kappa_{\boldsymbol{\mathcal{E}}}\rangle\!\rangle \overset{\text{def}}{=} \frac{1}{N}\sum_{K=1}^{N}\kappa_{\boldsymbol{\mathcal{E}}}^K, && \langle\!\langle\mu_{\boldsymbol{\mathcal{E}}}\rangle\!\rangle \overset{\text{def}}{=} \frac{1}{N}\sum_{K=1}^{N}\mu_{\boldsymbol{\mathcal{E}}}^K,\\
&\langle\!\langle\kappa_{\boldsymbol{\Sigma}}\rangle\!\rangle \overset{\text{def}}{=} \left(\frac{1}{N}\sum_{K=1}^{N}\frac{1}{\kappa_{\boldsymbol{\Sigma}}^K}\right)^{-1}, && \langle\!\langle\mu_{\boldsymbol{\Sigma}}\rangle\!\rangle \overset{\text{def}}{=} \left(\frac{1}{N}\sum_{K=1}^{N}\frac{1}{\mu_{\boldsymbol{\Sigma}}^K}\right)^{-1},
\end{aligned} \tag{2}$$

where the superscript K refers to the response from the Kth sample.

In order to determine a suitable RVE size, one must monitor the range of estimates to $\mathbb{E}^*$ for successively larger samples. This is depicted in Fig. 4. Relying on the

[6] For a tensor $\boldsymbol{A}$, $\|\boldsymbol{A}\| \overset{\text{def}}{=} \sqrt{\boldsymbol{A}\cdot\boldsymbol{A}}$.

[7] The distribution is controlled through the *random sequential addition process* [26], where the particles are placed sequentially and randomly into the volume. Homogenization results are insensitive to the volume shape or whether periodic boundary conditions were employed or not in the packing process, for sufficiently large number of particles.

[8] The sample size scales with the number of particles whenever the particle size is fixed.

[9] The purpose of using harmonic averaging for $\boldsymbol{\Sigma}$-related quantities is to be able to compute bounds on effective properties. See [11,29].

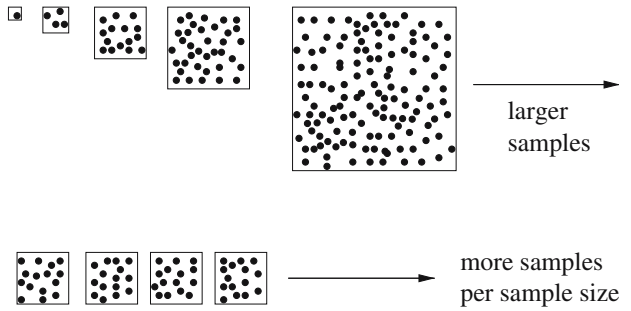

Fig. 4 Computationally, one considers successively larger samples, while many samples per sample size are tested

expectation that as $d/L \to 0$ (the RVE size increases indefinitely) the estimates will converge to $\mathbb{E}^*$, the following approach is used for computing an estimate. The method is outlined for linear displacement boundary conditions and the estimation of κ^* (one computes $\kappa_{\boldsymbol{\mathcal{E}}}$), where the following numerical convergence criterion is introduced. If P is the parameter being monitored for convergence, and K is an index for the sequence of parameters, convergence for the sequence P^K is declared when

$$\left| \frac{P^{K+1} - P^K}{P^K} \right| \leq \text{TOL}\,, \tag{3}$$

where TOL is a convergence tolerance. With this convergence criterion, to determine a suitable RVE size for a given heterogeneous material, one begins with a (small) sample size and ensemble averages from an increasing number of samples are compared until convergence is achieved to within a given tolerance. The ensemble average at convergence is denoted $\langle\!\langle \kappa_{\boldsymbol{\mathcal{E}}} \rangle\!\rangle$. Then, the sample size is successively enlarged and the ensemble averaging procedure is repeated for each sample size, creating a sequence of ensemble averages $\langle\!\langle \kappa_{\boldsymbol{\mathcal{E}}} \rangle\!\rangle^K$, where K is the index for sample size. The size of the sample at convergence of $\langle\!\langle \kappa_{\boldsymbol{\mathcal{E}}} \rangle\!\rangle^K$ is the required size to qualify as an RVE within the framework of this numerical method. Therefore, this procedure is essentially a method for quantifying a *numerical RVE size*, and will be revisited in homogenization in non-linear elasticity.

2.2 An example from linear elasticity

As an example to the homogenization process, an aluminum (matrix) and boron (particles) composite is analyzed. The macroscopic properties of a heterogeneous material are partially controlled by the material property contrast between the two phases. It is convenient to introduce *mismatch ratios* for material properties, which are defined as

$$m_\kappa \overset{\text{def}}{=} \frac{\kappa^2}{\kappa^1}, \qquad m_\mu \overset{\text{def}}{=} \frac{\mu^2}{\mu^1}\,. \tag{4}$$

The material properties for the composite are then given by the string

$$\{\kappa^1, \mu^1, m_\kappa, m_\mu, v_o^2\} = \{78\ \text{GPa}, 25\ \text{GPa}, 3, 7, 30\%\}.$$

Finite element mesh resolution is controlled by the number of (trilinear hexahedra) elements used in each direction to resolve a particle, denoted by N_m. The number of Gauss points used in each direction is denoted by N_g, yielding an $N_\text{g} \times N_\text{g} \times N_\text{g}$ integration grid. These parameters are depicted in Fig. 5. The following notes pertain to the numerical experiments:

1. For elements that have no material discontinuities $N_\text{g} = 2$ is sufficient. Elements that lie across matrix/particle interfaces will have jumps in the stress field, therefore higher order of integration is used for such elements. The effect of varying N_g for such elements is demonstrated with an example where a fixed sample with four particles is generated, and $\{\kappa_{\boldsymbol{\mathcal{E}}}, \mu_{\boldsymbol{\mathcal{E}}}\}$ are computed for successive refinement of the mesh for various values of N_g. Results are shown in Fig. 6. The effect of increasing N_g beyond $N_\text{g} = 3$ has a negligible effect on the numerical results, for meshes finer than $N_\text{m} = 4$. Therefore, $N_\text{g} = 3$ is used for elements with discontinuities in the rest of this section. The only parameter that controls numerical accuracy will therefore be N_m.
2. Regular meshes that do not conform to the geometry of the microstructure display slow convergence in numerical results with mesh refinement. To choose an appropriate mesh resolution, responses from samples with four particles is calculated (Fig. 7). After approximately $N_\text{m} = 5$, the scatter in sample responses for fixed N_m remains approximately constant in form, and the curve connecting sample responses for fixed N_m simply shifts down. Therefore, $N_\text{m} = 5$ is chosen as the mesh resolution.

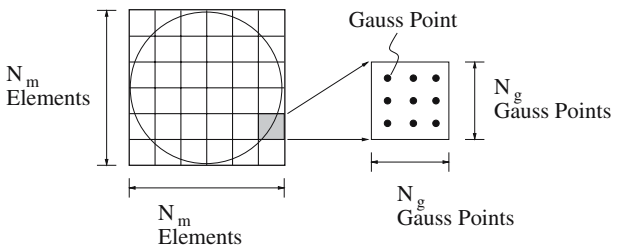

Fig. 5 Parameters N_g and N_m are depicted in two-dimensions. Mesh resolution is controlled by the number of elements per direction per particle (N_m). N_g Gauss points per direction is used in integration

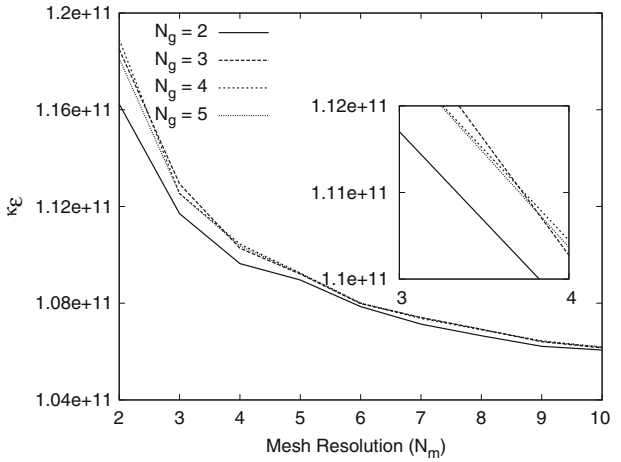

Fig. 6 Using a fixed sample with four particles, $\kappa_{\mathcal{E}}$ is computed for successively finer meshes (increasing N_{m}), for various orders of integration (N_{g}) in elements with material discontinuities. The effect of N_{g} for values greater than $N_{\mathrm{g}} = 3$ is negligible

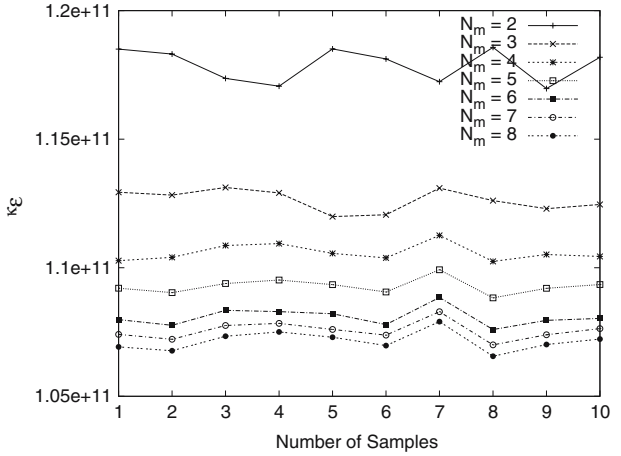

Fig. 7 For various mesh resolutions (N_{m}), ten samples are analyzed. Individual sample responses are connected with lines to emphasize the form of scatter. The form of scatter remains fixed after approximately $N_{\mathrm{m}} = 5$, and the response line simply shifts down

3. Tolerance for ensemble convergence is fixed to 5×10^{-3}. The scatter in sample responses for sample sizes larger than 100 particles were found to be very small, therefore a single sample was tested for such sample sizes.

Using Hill's energy criterion, one can argue [11,29] that ensemble averages $\{\langle\!\langle \kappa_{\mathcal{E}} \rangle\!\rangle, \langle\!\langle \mu_{\mathcal{E}} \rangle\!\rangle\}$ and $\{\langle\!\langle \kappa_{\Sigma} \rangle\!\rangle, \langle\!\langle \mu_{\Sigma} \rangle\!\rangle\}$ form, respectively, upper and lower bounds on the effective properties $\{\kappa^*, \mu^*\}$, and that with increasing sample size the bounds approach to each other. Results of the homogenization process are shown in Fig. 8, where the size of the samples was increased to 1,024 particles. Here, results are compared with analytical bounds,

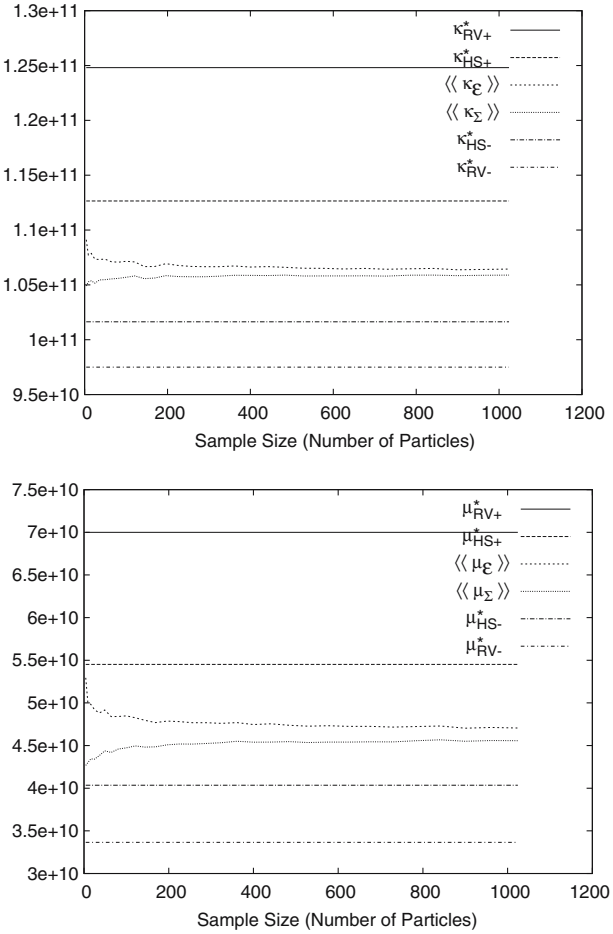

Fig. 8 Analytical bounds and linear elastic homogenization results for the aluminum–boron composite, with simulation parameters $\{\kappa^1, \mu^1, m_\kappa, m_\mu, v_o^2\} = \{78\ \mathrm{GPa}, 25\ \mathrm{GPa}, 3, 7, 0.3\}$

where RV−/RV+ denote the Reuss/Voigt bound and HS−/HS+ denote the Hashin-Shtrikman lower/upper bound. Results saturate at a sample size of approximately 400 particles. It is observed that a fixed gap remains between linear displacement and uniform traction boundary condition results. This can be explained with the mesh resolution employed, using a fixed sample with one particle (Fig. 9). With mesh refinement (increasing N_{m}) the gap between results from the two boundary conditions decrease and then saturate at large mesh resolutions. Therefore, if the homogenization process is repeated with a finer mesh resolution, one would expect the curves shown in Fig. 8 to display the behavior depicted in Fig. 10. Essentially, with increasing mesh resolution, the curves would shift down, while the remaining gap between homogenization results diminish, in the limit yielding $\langle\!\langle \kappa_{\mathcal{E}} \rangle\!\rangle = \kappa^* = \langle\!\langle \kappa_{\Sigma} \rangle\!\rangle$ and $\langle\!\langle \mu_{\mathcal{E}} \rangle\!\rangle = \mu^* = \langle\!\langle \mu_{\Sigma} \rangle\!\rangle$ for large samples as expected from the homogenization theory.

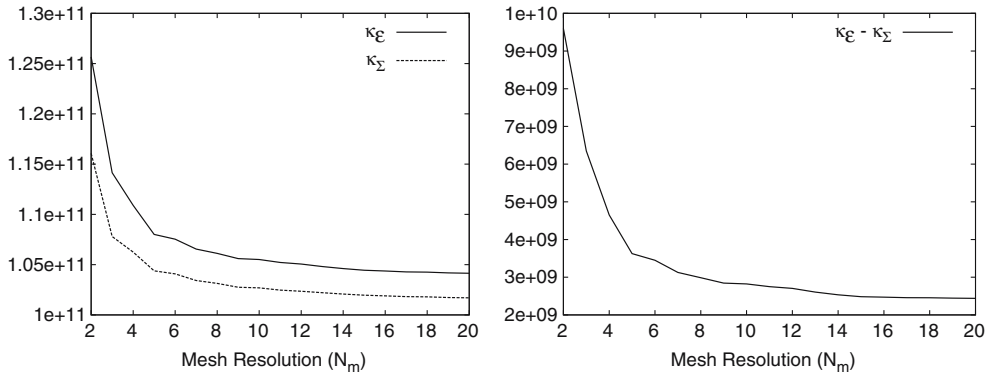

Fig. 9 Effect of mesh refinement on the gap between linear displacement and uniform traction boundary condition results. The gap between results from the two types of homogeneous boundary condition decreases and then saturates with increasing mesh resolution

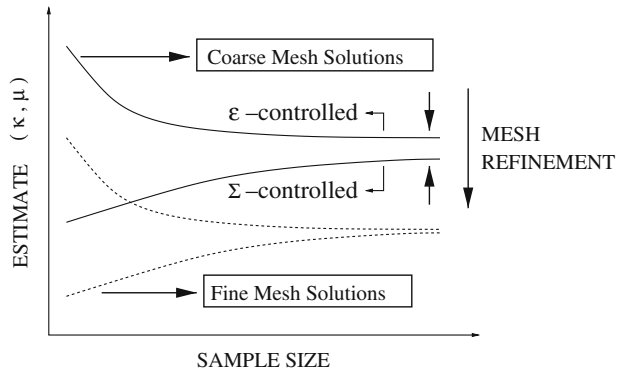

Fig. 10 With mesh refinement, it is expected that the curves corresponding to homogenization results will shift down, while the gap between the two types of homogeneous boundary conditions diminishes for large samples

3 Discrete material maps

In order to determine the explicit form of constitutive equations in non-linear elasticity experimentally, one has to conduct tension/compression/shear tests and fit a sufficiently smooth function to the data. For computational purposes, however, an explicit form of the constitutive equation is not necessary. In this section, a method is outlined by which one can directly incorporate material test data into the finite element procedure. This method will be used to characterize the macroscopic behavior of non-linearly deforming heterogeneous elastic materials. Attention is focused to isotropic homogeneous materials only.

3.1 Material testing

The most general form of the constitutive equation for an isotropic non-linearly elastic material is

$$\boldsymbol{S} = \alpha_0 \boldsymbol{I} + \alpha_1 \boldsymbol{E} + \alpha_2 \boldsymbol{E}^2 , \tag{5}$$

where $\boldsymbol{S}$ is the second Piola–Kirchhoff stress tensor, $\boldsymbol{E}$ is the Lagrangian strain, $\boldsymbol{I}$ is the identity tensor, and α_i are functions of the invariant set $\{I_{\boldsymbol{E}}, II_{\boldsymbol{E}}, III_{\boldsymbol{E}}\}$ of $\boldsymbol{E}$ only. This invariant set is uniquely determined by principal stretches $\lambda^i_{\boldsymbol{F}}$ of $\boldsymbol{F}$ for imposed deformations of the form $\boldsymbol{F} = \lambda^1_{\boldsymbol{F}} \boldsymbol{e}_1 \otimes \boldsymbol{E}_1 + \lambda^2_{\boldsymbol{F}} \boldsymbol{e}_2 \otimes \boldsymbol{E}_2 + \lambda^3_{\boldsymbol{F}} \boldsymbol{e}_3 \otimes \boldsymbol{E}_3$, which represents a tri-axial stretch as depicted in Fig. 11. The eigenvalues of $\boldsymbol{E}$ for this deformation are

$$\lambda^1_{\boldsymbol{E}} = \frac{1}{2}\left((\lambda^1_{\boldsymbol{F}})^2 - 1\right), \quad \lambda^2_{\boldsymbol{E}} = \frac{1}{2}\left((\lambda^2_{\boldsymbol{F}})^2 - 1\right),$$
$$\lambda^3_{\boldsymbol{E}} = \frac{1}{2}\left((\lambda^3_{\boldsymbol{F}})^2 - 1\right). \tag{6}$$

Suppose one conducted a material test on an isotropic material with unknown functions α_i, using the deformation described. The corresponding measured stress should have a diagonal form due to Eq. 5: $\boldsymbol{S} = \lambda^1_{\boldsymbol{S}} \boldsymbol{E}_1 \otimes \boldsymbol{E}_1 + \lambda^2_{\boldsymbol{S}} \boldsymbol{E}_2 \otimes \boldsymbol{E}_2 + \lambda^3_{\boldsymbol{S}} \boldsymbol{E}_3 \otimes \boldsymbol{E}_3$. Therefore, one immediately obtains three equations with three unknown coefficients α_i special to this deformation. In matrix form, these equations are:

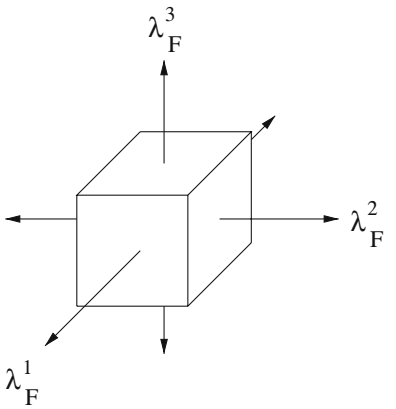

Fig. 11 Tri-axial stretch used in computational testing

$$\begin{bmatrix} 1 & \lambda_{\boldsymbol{E}}^1 & \left(\lambda_{\boldsymbol{E}}^1\right)^2 \\ 1 & \lambda_{\boldsymbol{E}}^2 & \left(\lambda_{\boldsymbol{E}}^2\right)^2 \\ 1 & \lambda_{\boldsymbol{E}}^3 & \left(\lambda_{\boldsymbol{E}}^3\right)^2 \end{bmatrix} \begin{Bmatrix} \alpha_0 \\ \alpha_1 \\ \alpha_2 \end{Bmatrix} = \begin{Bmatrix} \lambda_{\boldsymbol{S}}^1 \\ \lambda_{\boldsymbol{S}}^2 \\ \lambda_{\boldsymbol{S}}^3 \end{Bmatrix}. \tag{7}$$

If $\lambda_{\boldsymbol{F}}^i$ are distinct, then so are $\lambda_{\boldsymbol{E}}^i$ and $\lambda_{\boldsymbol{S}}^i$, so that these equations can be solved for α_i for this particular deformation.

3.2 Creating a material map

The set of α_i can be determined for a range of tri-axial stretches, thereby creating a *discrete material map* which characterizes the non-linear elastic material. The resolution of the map is determined by the stretch increments. In particular, if the range of deformations characterized by $\lambda_{\boldsymbol{F}}^i \in [\lambda_{\boldsymbol{F}}^{\min}, \lambda_{\boldsymbol{F}}^{\max}]$ are considered with stretch increments $\lambda_{\boldsymbol{F}}^{\text{inc}}$, the following algorithm determines the material map:

Algorithm for Creating a Material Map:

$\lambda_{\boldsymbol{F}}^1 = \lambda_{\boldsymbol{F}}^{\min}$

$\lambda_{\boldsymbol{F}}^2 = \lambda_{\boldsymbol{F}}^{\min} + a$

$\lambda_{\boldsymbol{F}}^3 = \lambda_{\boldsymbol{F}}^{\min} + a + b$

do $\left(\lambda_{\boldsymbol{F}}^1 = \lambda_{\boldsymbol{F}}^1 + \lambda_{\boldsymbol{F}}^{\text{inc}}\right)$ while $\left(\lambda_{\boldsymbol{F}}^1 \le \lambda_{\boldsymbol{F}}^{\max}\right)$

  do $\left(\lambda_{\boldsymbol{F}}^2 = \lambda_{\boldsymbol{F}}^2 + \lambda_{\boldsymbol{F}}^{\text{inc}}\right)$ while $\left(\lambda_{\boldsymbol{F}}^2 \le \lambda_{\boldsymbol{F}}^1 + a\right)$

    do $\left(\lambda_{\boldsymbol{F}}^3 = \lambda_{\boldsymbol{F}}^3 + \lambda_{\boldsymbol{F}}^{\text{inc}}\right)$ while $\left(\lambda_{\boldsymbol{F}}^3 \le \lambda_{\boldsymbol{F}}^2 + b\right)$

      calculate: $\{\lambda_{\boldsymbol{E}}^1, \lambda_{\boldsymbol{E}}^2, \lambda_{\boldsymbol{E}}^3\}$.

      measure: $\{\lambda_{\boldsymbol{S}}^1, \lambda_{\boldsymbol{S}}^2, \lambda_{\boldsymbol{S}}^3\}$.

      Note: $\boldsymbol{S} = \alpha_0 \boldsymbol{I} + \alpha_1 \boldsymbol{E} + \alpha_2 \boldsymbol{E}^2$

      solve and record: $\{\alpha_0, \alpha_1, \alpha_2\}$.

    end do

  end do

end do

In this algorithm, $\{a, b\} \ll \lambda_{\boldsymbol{F}}^{\text{inc}}$ are small offsets, used to avoid indeterminacy in the system of equations for α_i. Also, notice that $\lambda_{\boldsymbol{F}}^2$ is increased up to the current value of $\lambda_{\boldsymbol{F}}^1$, and $\lambda_{\boldsymbol{F}}^3$ is increased up to the current value of $\lambda_{\boldsymbol{F}}^2$, since spanning the whole range $[\lambda_{\boldsymbol{F}}^{\min}, \lambda_{\boldsymbol{F}}^{\max}]$ will result in the repetition of the invariants of $\boldsymbol{E}$, and therefore is redundant.

In the rest of this work, only two-dimensional formulations are considered, where the constitutive equations must have the form $\boldsymbol{S} = \alpha_0 \boldsymbol{I} + \alpha_1 \boldsymbol{E}$ so that there are only two coefficient functions to determine: α_o and α_1, where $\alpha_i = \widehat{\alpha}_i\{I_{\boldsymbol{E}}, I\!I_{\boldsymbol{E}}\}$. For hyper-elastic materials $\boldsymbol{S} = \partial \mathcal{W}/\partial \boldsymbol{E}$, where $\mathcal{W} = \widehat{\mathcal{W}}(I_{\boldsymbol{E}}, I\!I_{\boldsymbol{E}})$ is the strain energy function. The strain energy functions for three materials used in two dimensional examples are the compressible Mooney–Rivlin type material for which

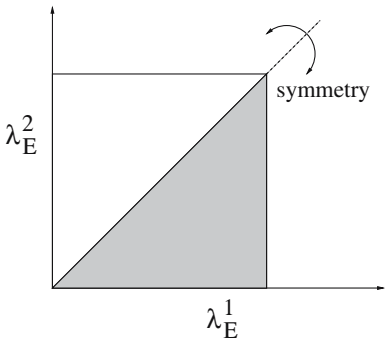

Fig. 12 Material maps generated are symmetric about the diagonal. Only the lower triangular portion is shown in figures. The invariants of $\boldsymbol{E}$ resulting from the upper triangular portion are a repetition of those from the lower triangular portion

$$\mathcal{W} = \frac{\mu}{2}\left(I_{\boldsymbol{C}} I\!I_{\boldsymbol{C}}^{-1/2} - 2\right) + \frac{\kappa}{2}\left(I\!I_{\boldsymbol{C}}^{1/2} - 1\right)^2, \tag{8}$$

where $\boldsymbol{C}$ is the right Cauchy-Green deformation tensor and μ, κ are the shear and bulk moduli, the Fung type material for which[10]

$$\mathcal{W} = C \exp\left(\alpha (I_{\boldsymbol{E}})^2 + \beta I\!I_{\boldsymbol{E}}\right) - C, \tag{9}$$

where C, $\alpha = (\lambda + 2\mu)/2C$, $\beta = -(2\mu/C)$ are material constants, and λ, μ are the Lame constants, and the Kirchhoff-St. Venant material for which $\boldsymbol{S} = \lambda\ \mathrm{tr}(\boldsymbol{E})\boldsymbol{I} + 2\mu\boldsymbol{E}$. These functions satisfy the fundamental requirements on the strain energy function, which are [5]: (i) $\mathcal{W} \ge 0$, (ii) $\boldsymbol{E} \to \boldsymbol{0} \Rightarrow \mathcal{W} \to 0$, (iii) $\boldsymbol{E} \to \boldsymbol{0} \Rightarrow \partial \mathcal{W}/\partial \boldsymbol{E} = \boldsymbol{S} \to 0$, and that (iv) $\boldsymbol{E} \to \boldsymbol{0} \Rightarrow \partial^2 \mathcal{W}/\partial \boldsymbol{E}^2 \to I\!I\!I\boldsymbol{E}$ (the linear elastic constitutive relationship should be recovered for the material).

Examples to material maps for two-dimensional cases are provided in Figs. 13, 14 and 15, using the test parameters listed in Table 1. Only the portion of the map that is computed is shown, due to symmetry about the diagonal axis (Figure 12).

3.3 Finite element implementation

In order to implement a discrete material map in the finite element procedure, one must guarantee the continuity of stresses generated from this map with

[10] This strain energy function, for three dimensional formulations, was originally proposed by [7] for lung tissue.

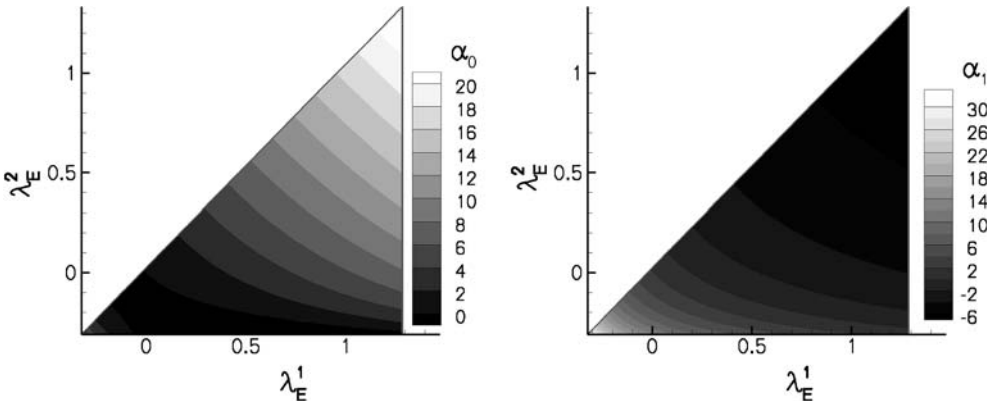

Fig. 13 Discrete material map for a Mooney-Rivlin material. See Table 1 for test parameters

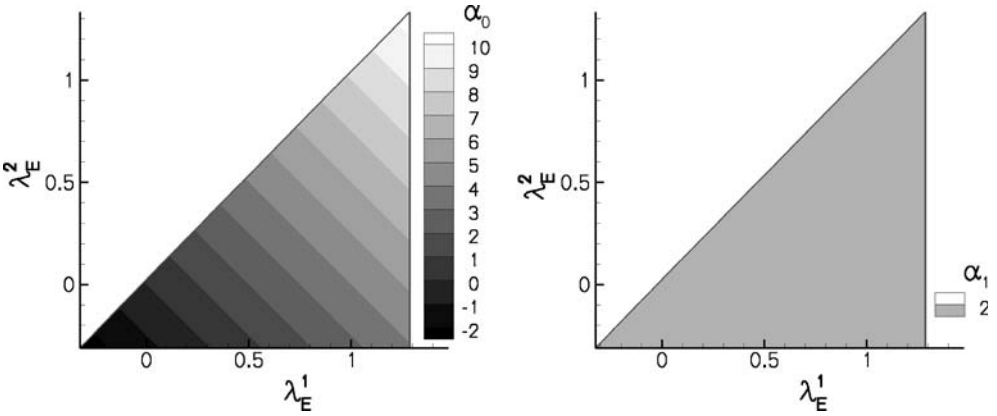

Fig. 14 Discrete material map for a Kirchhoff-St.Venant material. See Table 1 for test parameters

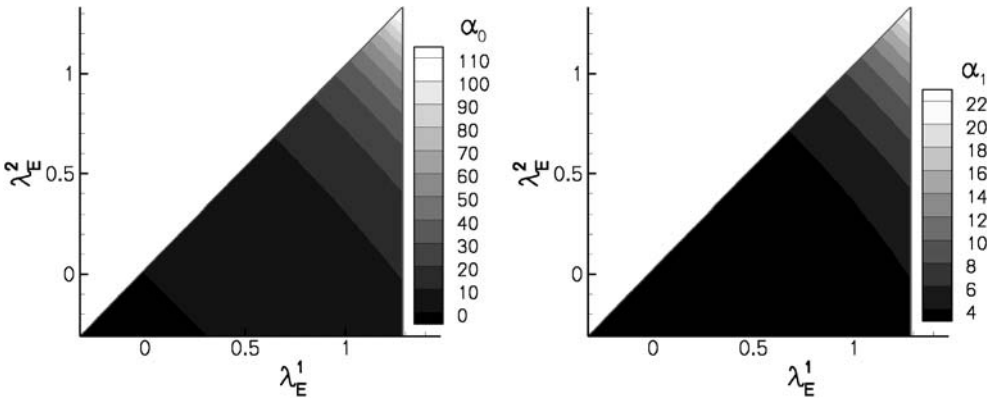

Fig. 15 Discrete material map for a Fung material. See Table 1 for test parameters. Decreasing the value of C leads to a steeper increase in α_i

respect to deformation. A continuous map may be generated through the interpolation of the data. In particular, a piecewise continuous interpolation may be used, where the data obtained for α_i is interpreted as being the set of nodal values for a finite element mesh, referred to as the *map mesh*, in the $\{\lambda^1_{\boldsymbol{E}}, \lambda^2_{\boldsymbol{E}}, \lambda^3_{\boldsymbol{E}}\}$ space. One would then obtain the piecewise linear interpolation (using summation convention)

Table 1 Test parameters used in calculations

$\lambda_{\boldsymbol{F}}^{\min}$	$\lambda_{\boldsymbol{F}}^{\max}$	$\lambda_{\boldsymbol{F}}^{\text{inc}}$	a	κ	μ	C
0.60	1.90	0.05	0.01	5	1	10

$$\begin{aligned}
\alpha_0(\lambda_{\boldsymbol{E}}^1,\lambda_{\boldsymbol{E}}^2,\lambda_{\boldsymbol{E}}^3) &= \alpha_0^I \Phi^I(\lambda_{\boldsymbol{E}}^1,\lambda_{\boldsymbol{E}}^2,\lambda_{\boldsymbol{E}}^3),\\
\alpha_1(\lambda_{\boldsymbol{E}}^1,\lambda_{\boldsymbol{E}}^2,\lambda_{\boldsymbol{E}}^3) &= \alpha_1^I \Phi^I(\lambda_{\boldsymbol{E}}^1,\lambda_{\boldsymbol{E}}^2,\lambda_{\boldsymbol{E}}^3),\\
\alpha_2(\lambda_{\boldsymbol{E}}^1,\lambda_{\boldsymbol{E}}^2,\lambda_{\boldsymbol{E}}^3) &= \alpha_2^I \Phi^I(\lambda_{\boldsymbol{E}}^1,\lambda_{\boldsymbol{E}}^2,\lambda_{\boldsymbol{E}}^3),
\end{aligned} \tag{10}$$

where I is the index for element nodes, $\{\alpha_0^I, \alpha_1^I, \alpha_2^I\}$ are nodal values, and Φ^I are a choice of standard finite element nodal shape functions.

This interpolation is easily implemented in the FEM analysis. For instance, the numerical tangent calculation in the FEM procedure requires the value of stress at the integration point, which is immediately determined through this interpolation, once one determines the eigenvalues $\{\lambda_{\boldsymbol{E}}^1, \lambda_{\boldsymbol{E}}^2, \lambda_{\boldsymbol{E}}^3\}$ of $\boldsymbol{E}$ at this point.

The map mesh, using triangular elements in the two-dimensional case, is shown in Fig. 16, using the test parameters listed in Table 1. Figure 16 also provides an example to the resulting piecewise linear interpolation of α_0 for the Fung material.

4 Homogenization in non-linear elasticity

In this section, methods for determining the RVE size and material characterization for non-linearly elastic deformations are introduced. Consider a heterogeneous material $\mathcal{M}$, associated with the reference configuration $\mathcal{R}_o$, with constitutive equation $\boldsymbol{S} = \widehat{\boldsymbol{S}}(\boldsymbol{X}, \boldsymbol{E})$. Attention is focused to heterogeneous materials that are composed of two isotropic materials, a matrix ($\mathcal{M}^1$) and particles ($\mathcal{M}^2$), which are characterized by their constitutive equations $\widehat{\boldsymbol{S}}^I(\boldsymbol{E})$. It is recalled that the constitutive equations have the general form $\widehat{\boldsymbol{S}}^I(\boldsymbol{E}) = \alpha_0^I \boldsymbol{I} + \alpha_1^I \boldsymbol{E} + \alpha_2^I \boldsymbol{E}^2$, where α_i^I are functions of the invariant set $\{I_{\boldsymbol{E}}, I\!I_{\boldsymbol{E}}, I\!I\!I_{\boldsymbol{E}}\}$ of $\boldsymbol{E}$.

To extract macroscopic information from a volume element $\mathcal{V}_o$ that qualifies as an RVE, linear displacement boundary conditions ($\boldsymbol{x} = \boldsymbol{\Phi X}$ on $\partial\mathcal{V}_o$, where $\boldsymbol{\Phi}$ is a constant tensor) and uniform traction boundary conditions are typically used ($\boldsymbol{p} = \boldsymbol{\Pi N}$ on $\partial\mathcal{V}_o$, where $\boldsymbol{\Pi}$ is a constant tensor). In linear elasticity, a single macroscopic measure ($I\!\boldsymbol{E}^*$) is sought, whereas such a measure does not exist in non-linear elasticity. Therefore, one instead looks for macroscopic stress and strain measures. These measures are the macroscopic 1st Piola-Kirchhoff stress tensor $\boldsymbol{P}^*$ and the macroscopic deformation gradient $\boldsymbol{F}^*$, which were first noted by [9]:

$$\boldsymbol{F}^* \overset{\text{def}}{=} \langle \boldsymbol{F} \rangle_{\mathcal{V}_o}, \qquad \boldsymbol{P}^* \overset{\text{def}}{=} \langle \boldsymbol{P} \rangle_{\mathcal{V}_o}. \tag{11}$$

For these identifications of macroscopic measures, one recovers a micro-macro energy balance in the rate form for the two types of boundary conditions noted;

$$\langle \boldsymbol{P} \cdot \dot{\boldsymbol{F}} \rangle_{\mathcal{V}_o} = \boldsymbol{P}^* \cdot \dot{\boldsymbol{F}}^*, \tag{12}$$

which is an extension of Hill's criterion to non-linear deformations.

The macroscopic identifications stated in Eq. 11 set the form for basic kinematic and kinetic quantities, and other ones must be derived, or *defined*, using these choices together with the usual continuum mechanics tools. The following identities are noted in particular:

Macroscopic kinematic and kinetic quantities:
If $\boldsymbol{F}^* \overset{\text{def}}{=} \langle \boldsymbol{F} \rangle_{\mathcal{V}_o}$ and $\boldsymbol{P}^* \overset{\text{def}}{=} \langle \boldsymbol{P} \rangle_{\mathcal{V}_o}$, then one obtains the kinematical quantities for the macroscopic material as

$$\begin{aligned}
&J^* = \det(\boldsymbol{F}^*), \qquad \boldsymbol{C}^* = (\boldsymbol{F}^*)^{\mathrm{T}} \boldsymbol{F}^*, \qquad \boldsymbol{B}^* = \boldsymbol{F}^* (\boldsymbol{F}^*)^{\mathrm{T}},\\
&\boldsymbol{E}^* = \frac{1}{2}(\boldsymbol{C}^* - \boldsymbol{I}), \qquad \boldsymbol{e}^* = \frac{1}{2}(\boldsymbol{I} - (\boldsymbol{B}^*)^{-1}),
\end{aligned} \tag{13}$$

and the kinetic quantities as

$$\boldsymbol{S}^* = (\boldsymbol{F}^*)^{-1} \boldsymbol{P}^*, \qquad \boldsymbol{T}^* = \frac{1}{J^*} \boldsymbol{P}^* (\boldsymbol{F}^*)^{\mathrm{T}}. \tag{14}$$

Whenever the microscopic constituents are hyper-elastic, the macroscopic material is also hyper-elastic with

$$\mathcal{W}^* \overset{\text{def}}{=} \langle \mathcal{W} \rangle_{\mathcal{V}_o}, \qquad \boldsymbol{P}^* = \frac{\partial \mathcal{W}^*}{\partial \boldsymbol{F}^*}, \qquad \boldsymbol{S}^* = \frac{\partial \mathcal{W}^*}{\partial \boldsymbol{E}^*}, \tag{15}$$

such that

$$\boldsymbol{E}^* \to \boldsymbol{0} \Rightarrow \frac{\partial^2 \mathcal{W}^*}{\partial (\boldsymbol{E}^*)^2} \to I\!\boldsymbol{E}^*. \tag{16}$$

The following remarks complement the definitions of macroscopic kinematic and kinetic measures as noted above [9,10].

1. The angular momentum balance for the macroscopic material is automatically satisfied since $\boldsymbol{T}^*$ can be shown to be symmetric. To show this, notice that for homogeneous boundary conditions the identity $\langle \boldsymbol{P}\boldsymbol{F}^T \rangle = \langle \boldsymbol{P} \rangle \langle \boldsymbol{F}^T \rangle$ holds.[11] Since $\langle \boldsymbol{P}\boldsymbol{F}^{\mathrm{T}} \rangle = \langle (1/J)\boldsymbol{T} \rangle$ and $\boldsymbol{T}$ is guaranteed to be symmetric, so is $\langle \boldsymbol{P}\boldsymbol{F}^T \rangle$. Therefore, $\boldsymbol{T}^* = 1/J^* \boldsymbol{P}^* (\boldsymbol{F}^*)^T = 1/\det(\langle \boldsymbol{F} \rangle) \langle \boldsymbol{P} \rangle \langle \boldsymbol{F}^T \rangle = 1/\det(\langle \boldsymbol{F} \rangle) \langle \boldsymbol{P}\boldsymbol{F}^{\mathrm{T}} \rangle$ is symmetric and the angular momentum balance is satisfied.

[11] See, e.g., [19] for proofs of similar identities.

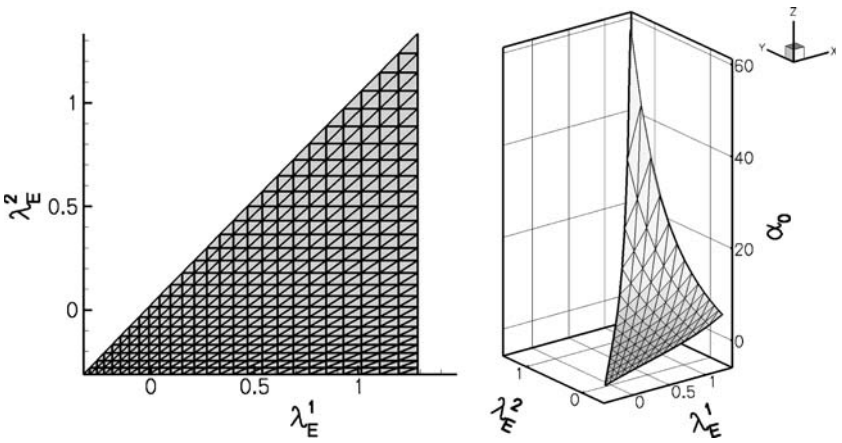

Fig. 16 An example to the map mesh (left), and the piecewise linearly interpolated α_0-map for the Fung material identified in Table 1 (right)

2. To prove the hyper-elasticity of the macroscopic material (provided the constituents are hyper-elastic), notice that if $\mathcal{W}^* = \langle \mathcal{W} \rangle_{\mathcal{V}_o}$ for all times, then $\dot{\mathcal{W}}^* = \langle \dot{\mathcal{W}} \rangle_{\mathcal{V}_o}$. It immediately follows from the micro-macro energy balance for homogeneous boundary conditions and the definitions of $\boldsymbol{P}^*$ and $\boldsymbol{F}^*$ that $\langle \dot{\mathcal{W}} \rangle_{\mathcal{V}_o} = \langle \boldsymbol{P} \cdot \dot{\boldsymbol{F}} \rangle_{\mathcal{V}_o} = \boldsymbol{P}^* \cdot \dot{\boldsymbol{F}}^* = \dot{\mathcal{W}}^*$. Now, $\mathcal{W}^*$ is a function of $\boldsymbol{F}^*$ only, so one immediately obtains $\dot{\mathcal{W}}^* = \partial \mathcal{W}^* / \partial \boldsymbol{F}^* \cdot \dot{\boldsymbol{F}}^* = \boldsymbol{P}^* \cdot \dot{\boldsymbol{F}}^*$. If this equality is to hold for all $\dot{\boldsymbol{F}}^*$, then $\boldsymbol{P}^* = \partial \mathcal{W}^* / \partial \boldsymbol{F}^*$ must hold for all $\boldsymbol{F}^*$, which completes the proof. The proof for $\boldsymbol{S}^* = \partial \mathcal{W}^* / \partial \boldsymbol{E}^*$ follows from fundamental continuum mechanics relationships.
3. The asymptotic behavior $\boldsymbol{E}^* \to \boldsymbol{0} \Rightarrow \partial^2 \mathcal{W}^* / \partial (\boldsymbol{E}^*)^2 \to \mathbb{E}^*$ states that for small strains, the macroscopic tangent modulus should approach the elasticity tensor of the macroscopic material, which is satisfied trivially.

It is also remarked that the identifications of alternative stress and strain measures through volumetric averaging, in particular $\boldsymbol{E}^* \overset{\text{def}}{=} \langle \boldsymbol{E} \rangle_{\mathcal{V}_o}$ and $\boldsymbol{S}^* \overset{\text{def}}{=} \langle \boldsymbol{S} \rangle_{\mathcal{V}_o}$, do not satisfy similar energy arguments, such as $\langle \boldsymbol{S} \cdot \dot{\boldsymbol{E}} \rangle_{\mathcal{V}_o} = \boldsymbol{S}^* \cdot \dot{\boldsymbol{E}}^*$, and therefore are not preferable. Also, linear displacement boundary conditions fit naturally into numerical schemes where displacement is the primary variable, which will be demonstrated shortly. Therefore, in the rest of this work, attention is focused to linear displacement boundary conditions.

4.1 Determination of the numerical RVE size

If the macroscopic material is isotropic, then its constitutive equation must be of the form

$$\boldsymbol{S}^* = \alpha_0^* \boldsymbol{I} + \alpha_1^* \boldsymbol{E}^* + \alpha_2^* (\boldsymbol{E}^*)^2 , \tag{17}$$

where $\alpha_i^* = \widehat{\alpha}_i^* (I_{\boldsymbol{E}^*}, \mathrm{II}_{\boldsymbol{E}^*}, \mathrm{III}_{\boldsymbol{E}^*})$. However, even for combinations of materials with very simple constitutive equations, it may not be possible to predict beforehand the explicit form of the constitutive equation for the macroscopic material. The macroscopic behavior can be characterized through data analysis from experiments, as described in Sect. 3. A prerequisite for such a task is the determination of a suitable test sample size (the numerical RVE size) for non-linearly elastic deformations.

4.1.1 Characterization of deformation in isotropic non-linear elasticity

To determine the numerical RVE size in non-linear elasticity, a procedure that can be specialized to linear elasticity is sought. To develop such a procedure, one may introduce two sets of invariants that imply each other uniquely for a symmetric tensor $\boldsymbol{A}$:

$$\{I_{\boldsymbol{A}}, \mathrm{II}_{\boldsymbol{A}}, \mathrm{III}_{\boldsymbol{A}}\} = \left\{ \mathrm{tr}(\boldsymbol{A}), \frac{1}{2}((\mathrm{tr}(\boldsymbol{A}))^2 - \mathrm{tr}\left(\boldsymbol{A}^2\right)), \det(\boldsymbol{A}) \right\},$$
$$\{I'_{\boldsymbol{A}}, \mathrm{II}'_{\boldsymbol{A}}, \mathrm{III}'_{\boldsymbol{A}}\} = \{ \mathrm{tr}(\boldsymbol{A}), \boldsymbol{A}' \cdot \boldsymbol{A}', \det(\boldsymbol{A}) \}. \tag{18}$$

Returning to linear elasticity, one can now write

$$\kappa = \frac{I'_{\boldsymbol{\sigma}}}{3 I'_{\boldsymbol{\epsilon}}}, \qquad \mu = \frac{(\mathrm{II}'_{\boldsymbol{\sigma}})^{1/2}}{2 (\mathrm{II}'_{\boldsymbol{\epsilon}})^{1/2}} , \tag{19}$$

the convergence of which was used to determine the numerical RVE size for linear homogenization. In order to generalize these convergence monitors to the non-linear regime, the following *characterization parameters* are introduced (for non-zero $\{I'_{\boldsymbol{E}}, \mathrm{II}'_{\boldsymbol{E}}, \mathrm{III}'_{\boldsymbol{E}}\}$):

$$\kappa \overset{\text{def}}{=} \frac{I'_{\boldsymbol{S}}}{3 I'_{\boldsymbol{E}}}, \qquad \mu \overset{\text{def}}{=} \frac{(\mathrm{II}'_{\boldsymbol{S}})^{1/2}}{2 (\mathrm{II}'_{\boldsymbol{E}})^{1/2}}, \qquad \pi \overset{\text{def}}{=} \frac{(\mathrm{III}'_{\boldsymbol{S}})^{1/3}}{(\mathrm{III}'_{\boldsymbol{E}})^{1/3}} . \tag{20}$$

Using $\{\kappa, \mu, \pi\}$ and $\boldsymbol{E}$, one can directly compute $\boldsymbol{S}$. In other words, $\{\kappa, \mu, \pi\}$ are alternatives to the functions $\{\alpha_0, \alpha_1, \alpha_2\}$. Note that κ and μ trivially simplify to the linear elastic material constants when deformations are small. Also, for two-dimensional analyses, one only needs two parameters, namely κ and μ.

4.1.2 Numerical RVE

To characterize the stress–strain state for an RVE, one simply replaces $\boldsymbol{S}$ and $\boldsymbol{E}$ with $\boldsymbol{S}^*$ and $\boldsymbol{E}^*$ in Eq. (20). Suppose the linear displacement boundary condition ($\boldsymbol{x} = \boldsymbol{\Phi X}$ on $\partial\mathcal{V}_o$) is specified on a volume element $\mathcal{V}_o$ *that qualifies as an RVE*. For this case, one may compute the following characterization parameters

$$\kappa^* \stackrel{\text{def}}{=} \frac{I'_{\boldsymbol{S}^*}}{3I'_{\boldsymbol{E}^*}}, \quad \mu^* \stackrel{\text{def}}{=} \frac{(I\!I'_{\boldsymbol{S}^*})^{1/2}}{2(I\!I'_{\boldsymbol{E}^*})^{1/2}}, \quad \pi^* \stackrel{\text{def}}{=} \frac{(I\!I\!I'_{\boldsymbol{S}^*})^{1/3}}{(I\!I\!I'_{\boldsymbol{E}^*})^{1/3}}. \quad (21)$$

In these equations $\boldsymbol{F}^* = \langle \boldsymbol{F} \rangle_{\mathcal{V}_o} = \boldsymbol{\Phi}$ due to an averaging theorem [9], therefore one obtains $\boldsymbol{E}^* = \frac{1}{2}(\boldsymbol{\Phi}^T\boldsymbol{\Phi} - \boldsymbol{I})$. Also, $\boldsymbol{P}^* = \langle \boldsymbol{P} \rangle_{\mathcal{V}_o}$ yields $\boldsymbol{S}^* = (\boldsymbol{F}^*)^{-1}\boldsymbol{P}^* = \boldsymbol{\Phi}^{-1}\langle \boldsymbol{P} \rangle_{\mathcal{V}_o}$.

$\boldsymbol{E}^*$ only depends on $\boldsymbol{\Phi}$. However, for samples smaller than the RVE size $\langle \boldsymbol{P} \rangle_{\mathcal{V}_o}$ is only an approximation to the actual $\boldsymbol{P}^*$ that characterizes the stress state of the macroscopic material for this deformation state. Therefore, the characterization parameters computed on a finite size sample, denoted by $\{\kappa_{\boldsymbol{\Phi}}, \mu_{\boldsymbol{\Phi}}, \pi_{\boldsymbol{\Phi}}\}$, are only approximations to $\{\kappa^*, \mu^*, \pi^*\}$. With this observation, the following procedure may be followed to determine a numerical RVE size for non-linear elastic deformations of heterogeneous materials:

1. One expects that if the typical dimension of $\mathcal{V}_o$ (L) is much larger than the typical dimension of a particle (d), in other words as $d/L \to 0$, the sample will resemble an RVE, and the approximations $\{\kappa_{\boldsymbol{\Phi}}, \mu_{\boldsymbol{\Phi}}, \pi_{\boldsymbol{\Phi}}\}$ will be accurate. Therefore, one may monitor the convergence of $\{\kappa_{\boldsymbol{\Phi}}, \mu_{\boldsymbol{\Phi}}, \pi_{\boldsymbol{\Phi}}\}$ to determine the numerical RVE size. Explicitly, one compares parameters $\{\kappa_{\boldsymbol{\Phi}}, \mu_{\boldsymbol{\Phi}}, \pi_{\boldsymbol{\Phi}}\}$ on successively larger samples, until they converge with respect to a specified convergence criterion. The final sample size is the numerical RVE size.
2. Small samples would be expected to display a wider range of responses compared to large samples. This situation may be remedied by ensemble averaging parameters $\{\kappa_{\boldsymbol{\Phi}}, \mu_{\boldsymbol{\Phi}}, \pi_{\boldsymbol{\Phi}}\}$ computed on different samples of a fixed sample size, until successsive ensemble averages converge with respect to a specified convergence criterion. Then, one would compare ensemble averages from successively larger samples to determine the numerical RVE size.

Aspects of sample enlargement and ensemble averaging will be investigated numerically in the next section.

Clearly, the numerical RVE size would be expected to depend on the particular form of deformation, specified by $\boldsymbol{\Phi}$. The procedure described above is a method of determining a suitable numerical RVE size *special to this deformation*. The estimate to $\boldsymbol{S}^*$ computed on the numerical RVE size may then be used to approximate the response of the macroscopic material. The deformation dependence of the RVE size is investigated in Sect. 5.3.

4.2 Solution to the macroscopic problem

The numerical procedure described can directly be incorporated into the FEM solution procedure. For quasi-static problems, and in the absence of body forces, the weak form for the macroscopic problem is to determine $\boldsymbol{x}^*(\boldsymbol{X}, t)$ so that

$$-\int_{\mathcal{R}_o} \frac{\partial \boldsymbol{w}}{\partial \boldsymbol{X}} \cdot \boldsymbol{P}^* \, \mathrm{d}V + \int_{\partial\mathcal{R}_o^{\boldsymbol{p}^*}} \boldsymbol{w} \cdot \bar{\boldsymbol{p}}^* \, \mathrm{d}A = 0 \quad (22)$$

is satisfied for all $\boldsymbol{w}$, subject to $\boldsymbol{x}^* = \bar{\boldsymbol{x}}^*$ and $\boldsymbol{w} = \boldsymbol{0}$ on $\partial\mathcal{R}_o^{\boldsymbol{x}^*}$.

It is recalled that an iterative solution procedure to an FEM problem begins with a guess solution $\boldsymbol{x}_0^*$ to $\boldsymbol{x}^*$, which essentially prescribes an initial guess $\boldsymbol{F}_0^*$ to the macroscopic deformation gradient $\boldsymbol{F}^*$ at the integration point of each finite element. If the macroscopic stress-strain relationship were known, then one would be able to immediately compute the initial guess $\boldsymbol{P}_0^*$ to the macroscopic stress $\boldsymbol{P}^*$. However, as explained previously, one does not have a macroscopic constitutive equation for $\boldsymbol{P}^*$. There are two options to proceed with the analysis:

1. To approximate $\boldsymbol{P}_0^*$ at an integration point, one may prescribe $\boldsymbol{F}_0^*$ as a boundary condition to the homogenization procedure (Fig. 17). Explicitly, one sets $\boldsymbol{\Phi} = \boldsymbol{F}_0^*$ and applies the numerical scheme presented in section 4.1.2 to compute the effective stress.[12] The effective stress is estimated on the numerical RVE size for this iteration through $\boldsymbol{P}_0^* = \langle \boldsymbol{P} \rangle_{\mathcal{V}_o}$. Due to the lack of a macroscopic constitutive equation, one would essentially have to go through the numerical scheme presented at each integration point of the finite element mesh, for each solution iteration, and for each increment of the boundary conditions.
2. One may initially determine the discrete material map for the heterogeneous material (referred to as the *effective material map*) in the manner described in Sect. 3, using a suitable numerical RVE size as the test sample. This map essentially provides an approximation to the unknown macroscopic constitutive equation, and can be used to approximate $\boldsymbol{P}_0^*$

[12] See [2,13,15] for examples.

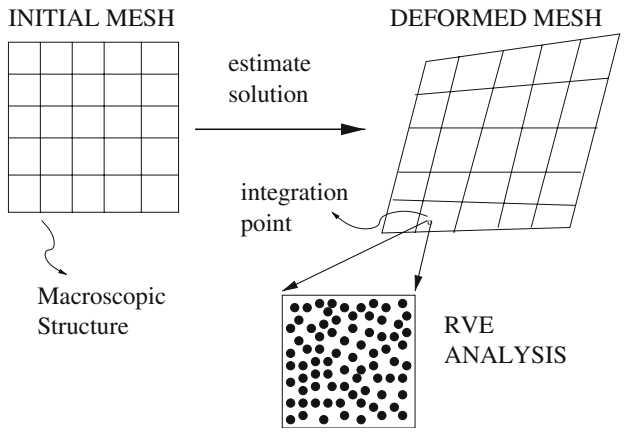

Fig. 17 Macroscopic analysis of a heterogeneous structure may be conducted by analyzing an RVE at each integration point

Table 2 Sample parameters used in calculations

κ^1	μ^1	C	m_κ	m_μ	v_o^2
5	1	10	3	7	0.40

for a given $\boldsymbol{F}_0^*$, without having to conduct additional RVE analyses.

In this work, the latter approach is taken. Therefore, the problem of non-linear homogenization is reduced to determining the effective material map. In this case, the test sample used to create the map may be chosen to be the largest numerical RVE size for the range of deformations considered to create the map. Then, the algorithm described in Sect. 3 may be applied to this test sample to determine estimates to $\{\alpha_0^*, \alpha_1^*, \alpha_2^*\}$ at each map node, and the map may be implemented in an FEM procedure in the manner described previously.

5 Numerical experiments

In this section, various aspects of the numerical RVE size determination and effective material map schemes are explored. Attention is focused on the effects of deformation. All analyses are conducted using two-dimensional models for efficient parameter analysis. The convergence criterion introduced in Sect. 2 is employed, and mismatch ratios m_κ and m_μ represent ratios of linear elasticity constants that appear explicitly in non-linear constitutive equations. In all simulations, fixed microstructural parameters tabulated in Table 2 are used, unless otherwise noted.

5.1 Isotropic inconsistencies

It is recalled that the constitutive equation for the macroscopic isotropic material must be of the form $\boldsymbol{S}^* = \alpha_0^* \boldsymbol{I} + \alpha_1^* \boldsymbol{E}^* + \alpha_2^* (\boldsymbol{E}^*)^2$. Therefore, $\boldsymbol{S}^*$ must be diagonal whenever $\boldsymbol{E}^*$ is diagonal. This observation may be used to investigate isotropic inconsistencies at finite deformations, since small samples that are not isotropic will yield a non-diagonal $\boldsymbol{S}^*$ for a diagonal $\boldsymbol{E}^*$. Explicitly, the following error monitors are used:

$$\text{£}^{\text{iso}} \overset{\text{def}}{=} \frac{\left\| \boldsymbol{S}^* - \boldsymbol{S}_D^* \right\|}{\left\| \boldsymbol{S}_D^* \right\|}, \qquad \langle\!\langle \text{£}^{\text{iso}} \rangle\!\rangle \overset{\text{def}}{=} \frac{\left\| \langle\!\langle \boldsymbol{S}^* - \boldsymbol{S}_D^* \rangle\!\rangle \right\|}{\left\| \langle\!\langle \boldsymbol{S}_D^* \rangle\!\rangle \right\|}, \quad (23)$$

where $\boldsymbol{S}_D^*$ is the tensor with diagonal entries of $\boldsymbol{S}^*$. If the sample is isotropic, $\boldsymbol{S}_D^* = \boldsymbol{S}^*$ and the error monitors are zero.

The variation of these error monitors is shown for two sample sizes in Fig. 18, using the microstructural parameters in Table 2 and $\boldsymbol{\Phi} = \boldsymbol{I} + 10^{-2}(1\boldsymbol{e}_1 \otimes \boldsymbol{E}_1 + 2\boldsymbol{e}_2 \otimes \boldsymbol{E}_2)$. Both the matrix and particles are Mooney-Rivlin materials. It is observed that ensemble averaging decreases isotropic inconsistencies rapidly for small samples, whereas large samples are already nearly representative of the macroscopic isotropic material. Therefore, when samples are large, one expects that a diagonal $\boldsymbol{E}^*$ will induce a nearly diagonal $\boldsymbol{S}^*$. It is remarked that this test would indicate an isotropic response when certain anisotropic materials' axes of symmetry (e.g. for transverse isotropy and orthotropy) line up with the axes of loading. However, this situation is hard to achieve for the class of particulate composites considered since random packing is employed.

5.2 Determining a numerical RVE size

The scheme outlined in Sect. 4 for determining a numerical RVE size *specific to a given deformation* is demonstrated, using 10^{-2} for all convergence tolerances. Consider a porous material, where the matrix is a Kirchhoff–St.Venant type material with properties and volume fraction of pores in Table 2. Samples are subjected to linear displacement boundary conditions with $\boldsymbol{\Phi} = \boldsymbol{I} + 10^{-1}\mathbf{1}$,[13] and the results are shown in Fig. 19. It is observed that the scatter in responses are larger for smaller sample sizes, and that ensemble averaging results display convergent behavior with increasing sample size. The simulation was stopped when both $\langle\!\langle \kappa_{\boldsymbol{\Phi}} \rangle\!\rangle$ and $\langle\!\langle \mu_{\boldsymbol{\Phi}} \rangle\!\rangle$ converged, from which one obtains a sample

[13] $\mathbf{1}$ is the tensor with all components equal to one with respect to the basis employed.

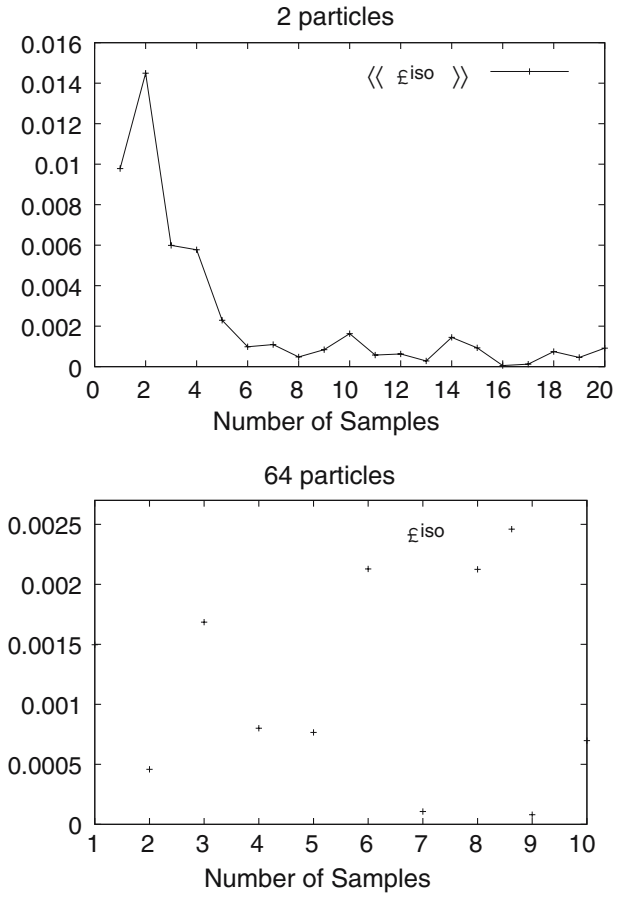

Fig. 18 Variation of isotropic inconsistencies with ensemble averaging. Matrix properties and mismatch ratios used are shown in Table 2. Both the matrix and particles are Mooney–Rivlin materials

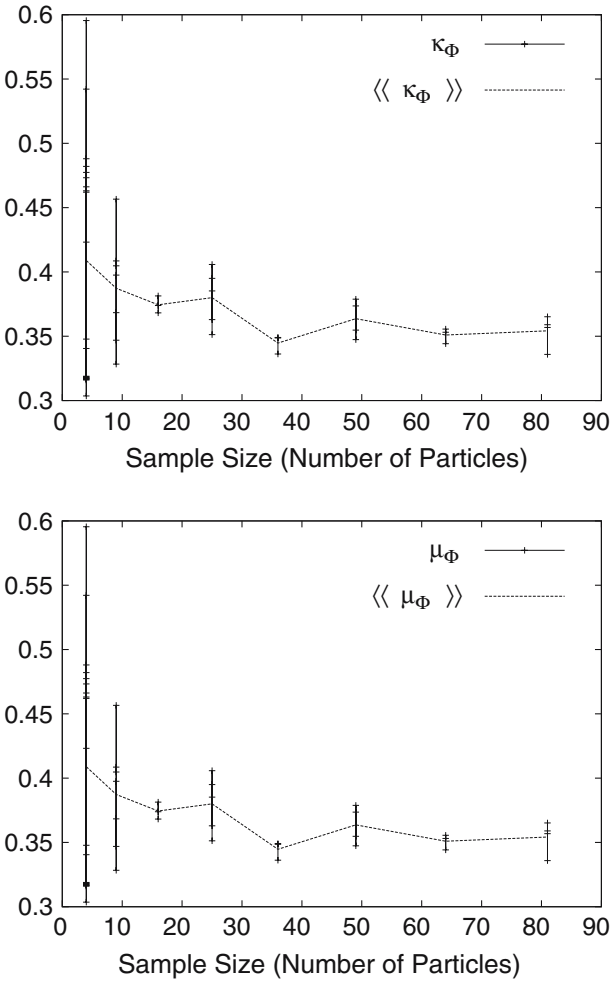

Fig. 19 Iterative RVE size determination scheme results. Matrix properties (Kirchhoff–St.Venant material) and volume fraction used are shown in Table 2. $\boldsymbol{\Phi} = \boldsymbol{I} + 10^{-1}\mathbf{1}$

size with 81 particles. Effects of ensemble averaging and variation of number of samples required with increasing sample size are shown in Fig. 20, where one observes again that with increasing number of samples ensemble averages converge quickly, and that larger samples typically require a smaller number of samples for convergence in ensemble averaging.

It is also noted that isotropic inconsistencies may result in dependence of convergence monitors explicitly on the form of $\boldsymbol{E}^*$, rather than only on its invariants. However, since large samples display negligible anisotropy, in the remaining portion of this work, this dependence is ignored and it is assumed that results depend on the invariants of $\boldsymbol{E}^*$ only.

5.3 Generation of an effective material map

Using the numerical schemes presented, one can calculate a discrete material map for the heterogeneous material characterized in Table 2, using Mooney–Rivlin materials for both the matrix and the particles, and the map parameters listed in Table 3, as described in Sect. 3. In order to do this, a suitable RVE size for map generation must be determined. The parameters employed in the RVE size determination scheme are functions of the deformation, which renders the associated RVE size deformation dependent. Figure 21 shows the variation of the numerical RVE size throughout the range of deformations considered. The numerical RVE size has less than or equal to 64 particles at all nodes of the map, except at a single node where the number of particles is 81. To determine the material map, RVE size is chosen to have 64 particles. The resulting map is shown in Fig. 22. Also, using the same RVE size of 64

Table 3 Material map generation parameters used throughout this section, unless otherwise noted. See Section 3 for details on map generation

$\lambda_{\boldsymbol{F}}^{\min}$	$\lambda_{\boldsymbol{F}}^{\max}$	$\lambda_{\boldsymbol{F}}^{\text{inc}}$	a	b
0.7	1.5	0.1	0.01	0.025

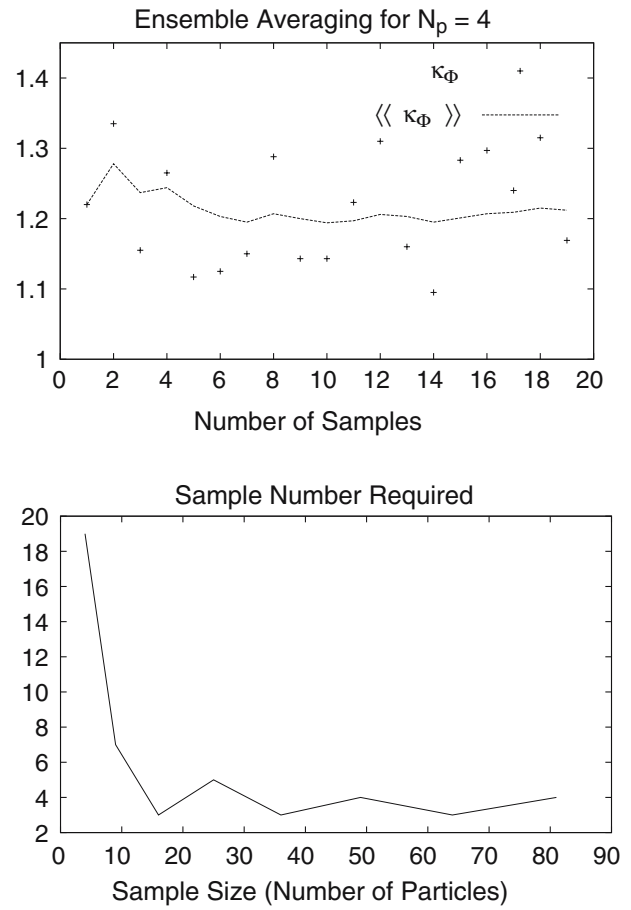

Fig. 20 Effects of ensemble averaging and variation of number of samples required with increasing sample size corresponding to results shown in Fig. 19

particles without verification, effective material maps for same microstructural parameters, but combination of two Kirchhoff–St.Venant materials and two Fung type materials are shown in Fig. 23 and 24. It should be noted that the behavior displayed in Fig. 23 for the combination of two Kirchhoff–St.Venant materials is not similar to that of a Kirchhoff–St.Venant material. Moreover, if the constitutive equations for the two materials are not of the same type, then there is no apparent candidate for an approximate constitutive equation. As an example, consider the microstructural parameters given in Table 2, using a Mooney-Rivlin type material as the matrix, and a Kirchhoff–St.Venant type material for the particles. The resulting material maps are shown in Fig. 25.

5.4 An application

The discrete material generated in Sect. 5.3 can be used in the analysis of a structure made of this heterogeneous material (Fig. 26). Consider a structure with voids in the reference configuration $\mathcal{R}_o$, subjected to linear displacement boundary conditions of the form $\boldsymbol{x} = \boldsymbol{\Phi X}$ on the outer boundary, where $[\boldsymbol{\Phi}] = \begin{bmatrix} 1.1 & 0.05 \\ 0.02 & 1.1 \end{bmatrix}$. The matrix material is represented by the discrete map of Fig. 22. It is assumed that the microstructure is sufficiently small with respect to the size of the structure, so that a homogenized solution is applicable. Results are shown in Fig. 27, where the mesh[14] resolution on the reference configuration $\mathcal{R}_o$ and the distribution of $\|\boldsymbol{P}^*\|$ on the deformed configuration $\mathcal{R}^*$ are given.

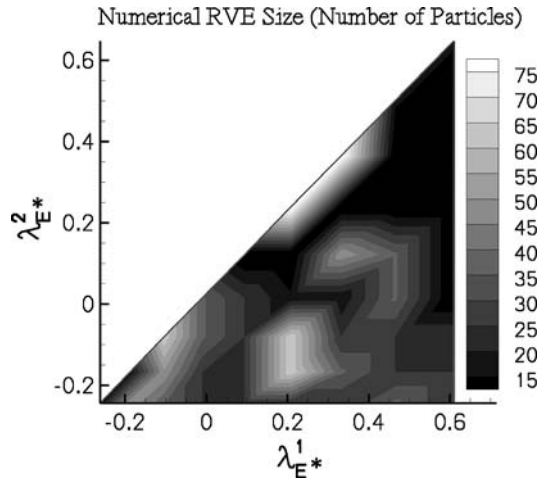

Fig. 21 The numerical RVE size map for material and map parameters listed in Tables 2 and 3, using Mooney-Rivlin materials

5.5 Comparison of computation time

Suppose one attempted to analyze the previous problem by analyzing an RVE at each integration point of the mesh as described in Sect. 4.2, by fixing the RVE size to $N_p = 64$. At the resolution shown in Fig. 27, the number of elements was $N_e = 1066$. Numerical generation of the stiffness matrix requires 7 RVE analyses per element, per Newton iteration. Each RVE analysis takes on the order of 40 s to complete on a standard workstation,[15] which means approximately 83 hours per Newton iteration. Assuming a total of 5–10 N iterations typically required for convergence, the total computation time required amounts to more than 3 weeks. The computation time required for the solution given in the previous section was 2.5 s, which is a significant improvement.

It is noted that the computation time required for the generation of the material map scales with the resolu-

[14] The triangular mesh generator *Triangle* by J. R. Shewchuk of University of California, Berkeley (USA) was used.

[15] This is calculated for a sample size of $N_p = 64$, subjected to linear displacement boundary conditions with $\boldsymbol{\Phi} = \boldsymbol{I} + 10^{-2}\boldsymbol{1}$.

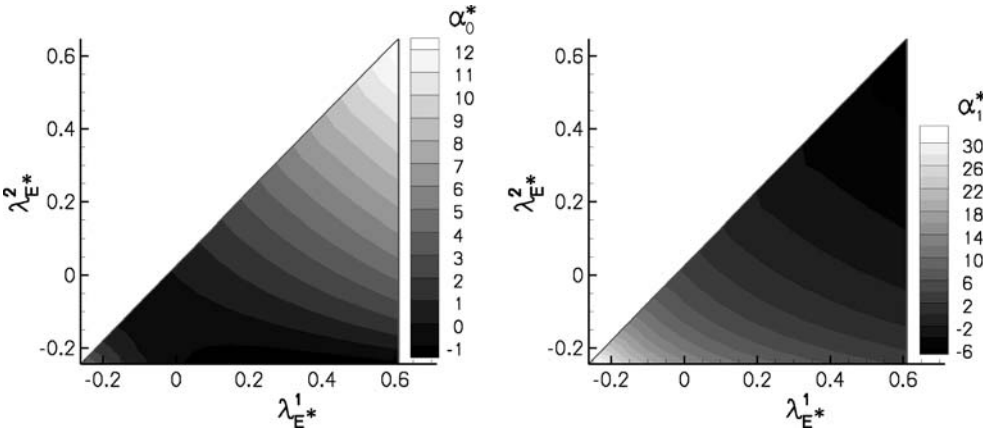

Fig. 22 Effective material maps for material and map parameters listed in Tables 2 and 3, using Mooney–Rivlin type materials. The mesh resolution is set to $\lambda_{\boldsymbol{F}}^{\text{inc}} = 0.05$

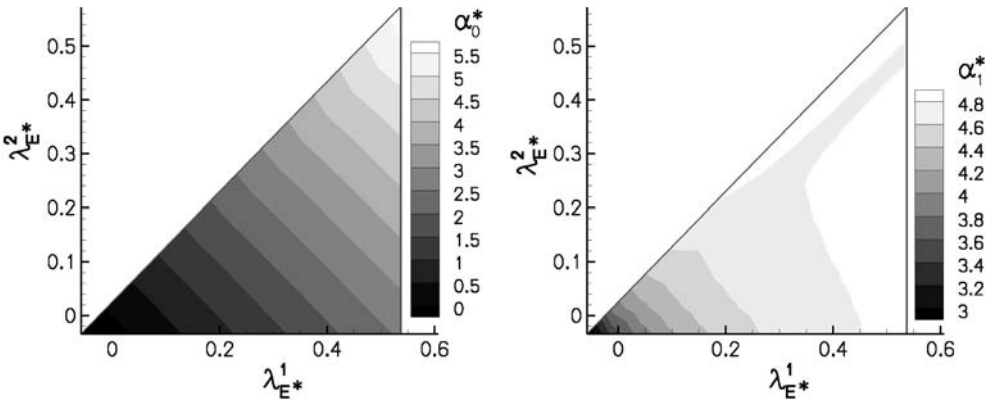

Fig. 23 Effective material maps for material parameters listed in Table 2, using Kirchhoff–St.Venant type materials. The mesh resolution is set to $\lambda_{\boldsymbol{F}}^{\text{inc}} = 0.05$, and $\{\lambda_{\boldsymbol{F}}^{\min}, \lambda_{\boldsymbol{F}}^{\max}\} = \{0.95, 1.45\}$.

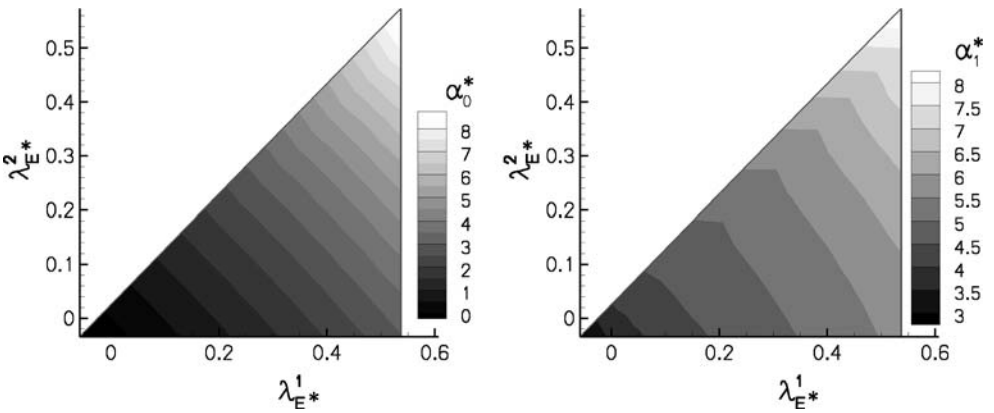

Fig. 24 Effective material maps for material parameters listed in Table 2, using Fung type materials. The mesh resolution is set to $\lambda_{\boldsymbol{F}}^{\text{inc}} = 0.05$, and $\{\lambda_{\boldsymbol{F}}^{\min}, \lambda_{\boldsymbol{F}}^{\max}\} = \{0.95, 1.45\}$.

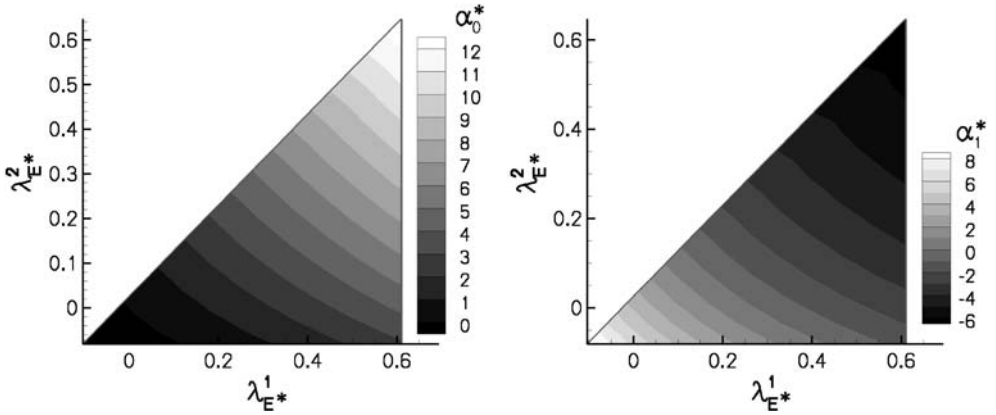

Fig. 25 Effective material maps for material parameters listed in Table 2, using a Mooney–Rivlin type material as the matrix, and a Kirchhoff–St.Venant type material for the particles. The mesh resolution is set to $\lambda_{\boldsymbol{F}}^{\text{inc}} = 0.05$, and $\{\lambda_{\boldsymbol{F}}^{\min}, \lambda_{\boldsymbol{F}}^{\max}\} = \{0.9, 1.50\}$

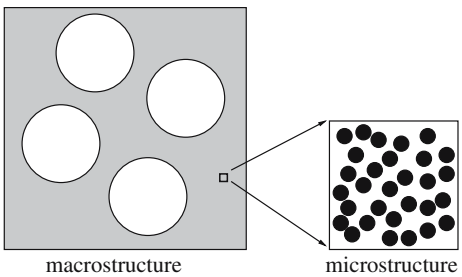

Fig. 26 The macroscopic structure is porous, where the matrix is a heterogeneous material

tion of the map. The computation of the map employed in this example required 153 RVE analyses, which corresponds to a computation time of 1.7 h with 40 s per RVE analysis. However, a single map may be applicable to multiple structural problems, or to the same problem with a different mesh resolution, which adds further efficiency to the method.

6 Conclusion

In this work, homogenization of linearly and non-linearly deforming heterogeneous elastic materials was investigated, using particle–matrix composites. The aim in both regimes is to estimate, or generate bounds for, the effective properties of the macroscopic material using an RVE. To determine an RVE size numerically for fixed microstructural parameters, one compares ensemble averaged parameters from successively larger sample sizes until results saturate to within a given tolerance. For overall isotropic behavior, the parameters monitored for convergence are the two material parameters (κ and μ) in the linear regime, and they are the three stress-strain characterization parameters (κ, μ and π) in the non-linear regime.

In the linear regime, the homogenization process was reviewed, and a method for determining a suitable RVE size was introduced based on the convergence behavior of homogenization parameters. In the non-linear regime, proper identification of macroscopic stress and strain was discussed, and three stress-strain characterization parameters (κ, μ and π) were introduced to extend the homogenization process in the linear regime to the non-linear regime. Attention was focused to the effects of deformation on the homogenization process, a factor that is not relevant for the linear regime. Monitoring of these parameters in convergence analysis (in determining the number of samples per sample size for ensemble averaging, and in comparing ensemble averages from successively larger sample sizes) was used successfully in numerically determining the RVE size. The RVE sizes for the range of deformations considered (which is characterized by the range of variation of the invariants of the strain tensor $\boldsymbol{E}$) were determined and, subsequently, a sample size was chosen to characterize the non-linear behavior of the heterogeneous material through the use of an effective material map. It was observed that combinations of materials with known (and relatively simple) constitutive equations may yield macroscopically non-trivial constitutive behaviors. Incorporation of the effective material map in the non-linear analysis of a microscopically heterogeneous macrostructure was found to significantly reduce the computation time.

Bifurcation phenomena, such as buckling on the microscale, were excluded from the analysis in this work. Whenever such phenomena are present, the RVE size employed to characterize the macroscopic behavior of the heterogeneous material must be critically evaluated.

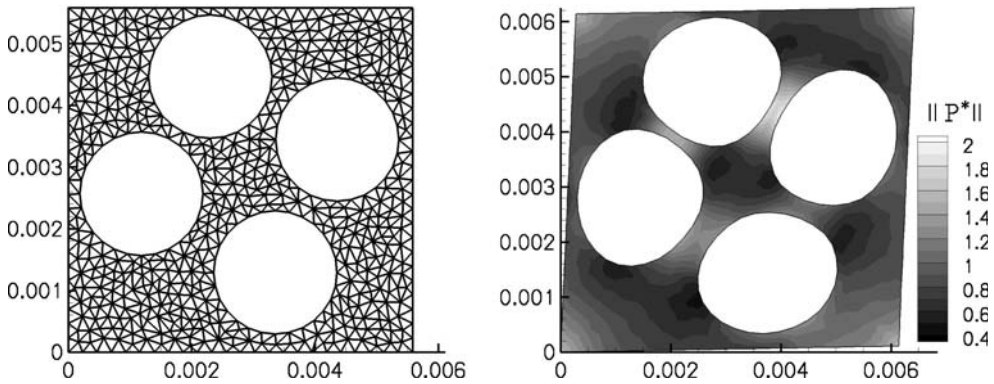

Fig. 27 Mesh resolution on the reference configuration $\mathcal{R}_o$ (left), and the distribution of $\|\boldsymbol{P}^*\|$ on $\mathcal{R}^*$

In particular, it has been shown that bifurcation phenomena may only be captured when a sufficiently large RVE size is employed [16,22] The RVE size determination scheme described in this work may require modification to incorporate such bifurcation effects.

The map resolution that is required for an accurate analysis of the macrostructure is a subject for future work. One may build a numerical criterion to make such a decision in the following way. Suppose, one computes a series of stress fields $\boldsymbol{P}^K$ for successively finer material maps, where K is the index for map refinement. On the reference configuration $\mathcal{R}_o$ of the macrostructure, one could then compute a relative error measure for the $K+1$-st stress field using an error monitor $\pounds_{\boldsymbol{P}}^K$:

$$\pounds_{\boldsymbol{P}}^K \stackrel{\text{def}}{=} \frac{\left\|\boldsymbol{P}^{K+1}-\boldsymbol{P}^K\right\|_{\mathcal{R}_o}}{\left\|\boldsymbol{P}^K\right\|_{\mathcal{R}_o}},$$

where $\|\boldsymbol{A}\|_{\mathcal{R}_o} = \int_{\mathcal{R}_o} \boldsymbol{A}\cdot\boldsymbol{A}\,\mathrm{d}V$ for a tensor $\boldsymbol{A}$. One could use this criterion to refine the material map and recompute the stress field, until the error decreases below a given tolerance: $\pounds_{\boldsymbol{P}}^K \le \mathrm{TOL}$.

The concept of a material map may also be extended to investigate the behavior of macroscopically anisotropic non-linearly elastic composites. For instance, the stress-strain relationship of a transversely isotropic material can be expressed as [14]

$$\boldsymbol{S}(\boldsymbol{C},\boldsymbol{n}) = \phi_0\boldsymbol{I}+\phi_1\boldsymbol{C}+\phi_2\boldsymbol{C}^2+\phi_3\boldsymbol{n}\otimes\boldsymbol{n}+\phi_4(\boldsymbol{n}\otimes \boldsymbol{C}\boldsymbol{n}+\boldsymbol{C}\boldsymbol{n}\otimes\boldsymbol{n})+\phi_5\boldsymbol{C}\boldsymbol{n}\otimes\boldsymbol{C}\boldsymbol{n},$$

where $\boldsymbol{n}$ is a vector normal to the plane of isotropy, and each coefficient function ϕ_i is represented by a function of the form $\phi_i = \widehat{\phi}_i(\,\mathrm{tr}(\boldsymbol{C}),\,\mathrm{tr}\left(\boldsymbol{C}^2\right),\,\mathrm{tr}\left(\boldsymbol{C}^3\right),\boldsymbol{n}\cdot\boldsymbol{C}\boldsymbol{n},\boldsymbol{n}\cdot\boldsymbol{C}^2\boldsymbol{n})$. Application of this form to a heterogeneous material that displays transverse isotropy on the macroscale would require a procedure for the determination of the effective coefficient functions ϕ_i^*, and is a subject of current research of the authors.

References

1. Aboudi J (1991) Mechanics of composite materials: a unified micromechanical approach. Elsevier, Amsterdam
2. Brieu M, Devries F (1999) Micro-mechanical approach and algorithm for the study of damage appearance in elastomer composites. Comp Struct 46:309–319
3. Castañeda PP (1989) The overall constitutive behavior of nonlinearly elastic composites. Proc R Soc Lond A 422(1862):147–171
4. Christensen RM (1991) Mechanics of composite materials. Krieger, New York
5. Ciarlet PG (1993) Mathematical elasticity: three dimensional elasticity. North-Holland, Amsterdam
6. Cioranescu D, Donato P (1998) An introduction to homogenization. Oxford University Press, New York
7. Fung YC (1993) Biomechanics: mechanical properties of living tissues, 2nd edn. Springer, Berlin Heidelberg New York
8. Hashin Z (1983) Analysis of composite materials. J Appl Mech 50:481–505
9. Hill R (1972) On constitutive macro-variables for heterogeneous solids at finite strain. Proc R Soc Lond A 326(1565):131–147
10. Hill R, Rice JR (1973) Elastic potentials and the structure of inelastic constitutive laws. SIAM J Appl Math 25(3):448–461
11. Huet C (1990) Application of variational concepts to size effects in elastic heterogeneous bodies. J Mech Phys Solids 38(6):813–841
12. Kanit T, Forest S, Galliet I, Mounoury V, Jeulin D (2003) Determination of the size of the representative volume element for random composites: statistical and numerical approach. Int J Solids Struct 40:3647–3679
13. Kouznetsova V, Brekelmans WAM, Baaijens FPT (2001) An approach to micro–macro modeling of heterogeneous materials. Comput Mech 27:37–48
14. Liu I-S (2002) Continuum mechanics. Springer, Berlin Heidelberg New York
15. Miehe C, Schotte J, Schröder J (1999) Computational micro-macro transitions and overall moduli in the analysis of polycrystals at large strains. Comput Materials Sci 16:372–382
16. Miehe C, Schröder J, Becker M (2002) Computational homogenization analysis in finite elasticity: material and structural

instabilities on the micro- and macro-scales of periodic composites and their interaction. Comput Methods Appl Mech Eng 191:4971–5005
17. Müller S (1987) Homogenization of nonconvex integral functionals and cellular elastic materials. Arch Ration Mech Anal 25:189–212
18. Mura T (1987) Micromechanics of defects in solids. Martinus Nijhoff, The Hague
19. Nemat-Nasser S (2004) Plasticity: a treatise on finite deformation of heterogeneous inelastic materials. Cambridge University Press, Cambridge.
20. Nemat-Nasser S, Hori M (1999) Micromechanics: overall properties of heterogeneous materials, 2nd edn. North-Holland, Amsterdam
21. Ogden RW (1978) Extremum principles in non-linear elasticity and their application to composites–i. Int J Solids Struct 14:265–282
22. Saiki I, Terada K, Ikeda K, Hori M (2002) Appropriate number of unit cells in a representative volume element for microstructural bifurcation encountered in a multi-scale modeling. Comput Methods Appl Mech Eng 191:2561–2585
23. Stroeven M, Askes H, Sluys LJ (2004) Numerical determination of representative volumes for granular materials. Comput Methods Appl Mech Eng 193:3221–3238
24. Sugimoto T (2001) Monodispersed particles. Elsevier, Amsterdam
25. Talbot DRS, Willis JR (1985) Variational principles for inhomogeneous non-linear media. IMA J Appl Math 35:39–54
26. Torquato S (2002) Random heterogeneous materials: microstructure and macroscopic properties. Springer, Berlin Heidelberg New York
27. Willis JR (1994) Upper and lower bounds for non-linear composite behavior. Materials Sci Eng A175:7–14
28. Zohdi TI, Wriggers P (2005) Introduction to computational micromechanics. Springer, Berlin Heidelberg New York
29. Zohdi T, Wriggers P, Huet C (2001) A method of substructuring large-scale computational micromechanical problems. Comput Methods Appl Mech Eng 190:5636–5656